Journal of Microscopy, Vol. 214, Pt 3 June 2004, pp. 315–327
Received 29 April 2003; accepted 31 October 2003

X-ray omni microscopy

D. PAGANIN*†, T. E. GUREYEV*, S. C. MAYO*,
A. W. STEVENSON*, YA. I. NESTERETS* & S. W. WILKINS*
**Commonwealth Scientific and Industrial Research Organization, Manufacturing and Infrastructure Technology, Private Bag 33, Clayton South, Victoria 3169, Australia*
†*School of Physics and Materials Engineering, Monash University, Victoria 3800, Australia*

Key words. Holography, phase contrast, phase retrieval, point-projection microscopy, X-ray microscopy.

Summary

The science of wave-field phase retrieval and phase measurement is sufficiently mature to permit the routine reconstruction, over a given plane, of the complex wave-function associated with certain coherent forward-propagating scalar wave-fields. This reconstruction gives total knowledge of the information that has been encoded in the complex wave-field by passage through a sample of interest. Such total knowledge is powerful, because it permits the emulation in software of the subsequent action of an infinite variety of coherent imaging systems. Such 'virtual optics', in which software forms a natural extension of the 'hardware optics' in an imaging system, may be useful in contexts such as quantitative atom and X-ray imaging, in which optical elements such as beam-splitters and lenses can be realized in software rather than optical hardware. Here, we develop the requisite theory to describe such hybrid virtual-physical imaging systems, which we term 'omni optics' because of their infinite flexibility. We then give an experimental demonstration of these ideas by showing that a lensless X-ray point projection microscope can, when equipped with the appropriate software, emulate an infinite variety of optical imaging systems including those which yield interferograms, Zernike phase contrast, Schlieren imaging and diffraction-enhanced imaging.

1. Introduction

The Fresnel diffraction integral allows one to determine how the complex disturbance of a given paraxial monochromatic scalar radiation wave-field (or mono-energetic scalar matter wave-field) will propagate through free space, to a plane downstream of the plane over which the wave-field was specified (Cowley, 1981). This diffraction integral is an approximation that may be derived from the Kirchhoff or Rayleigh–Sommerfeld diffraction integrals, which solve different boundary value problems for the time-independent scalar wave equation (Helmholtz equation) without introducing the paraxial approximation (Nieto-Vesperinas, 1991).

The Fresnel, Kirchhoff and Rayleigh–Sommerfeld free-space diffraction integrals are transforms that relate a given 'input' (the unpropagated wave-field, and/or its normal derivative, over some specified plane) to an 'output' (the propagated wave-field, over some specified plane). One may similarly view the integral transforms describing the action of certain coherent optical imaging systems: for example, the transfer function formalism relates the 'input' wave-field to be imaged, to the 'output' wave-field produced by an aberrated shift-invariant coherent linear imaging system (Goodman, 1968). Note that a shift-invariant linear imaging system is defined as an imaging system for which: (i) an arbitrary linear superposition of two inputs yields the same linear superposition of corresponding outputs; and (ii) a transverse shift in the input wave-field yields a transverse shift in the output wave-field, with the shift in the output wave-field being proportional to the shift in the input wave-field (Papoulis, 1968).

In all of the above examples, specification of the input complex wave-field (and/or its normal derivative) over a plane allows the output complex wave-field to be computed; this then allows one to compute the image (intensity map) as the square modulus of the output complex wave-function. For the remainder of the paper, we restrict ourselves to consideration of scenarios in which specification of the input complex wave-field, alone, provides sufficient information to determine the output image. Although the 'computation' of this output image is typically achieved using optical hardware such as lenses and imaging devices, it can also be achieved using optical software that numerically implements the relevant integral transforms, if the input wave-function is known.

This 'if' contains a problem, because the frequencies of complex electromagnetic disturbances at optical and shorter

Correspondence: Dr D. Paganin. Tel.: +61 39545 2702; fax: +61 39544 1128; e-mail: David.Paganin@csiro.au

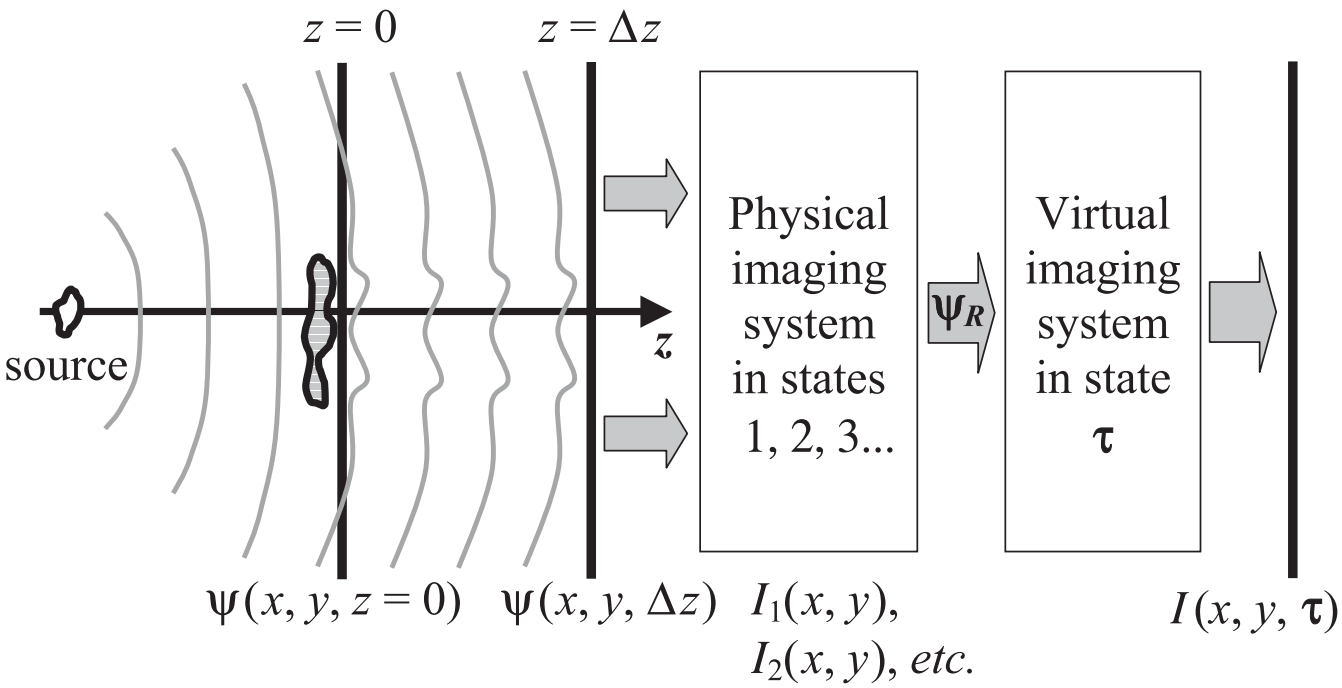

Fig. 1. Example of a hybrid virtual–physical imaging system. A given source leads to a well-characterized coherent wave-field; in this case we show a point source producing spherical waves. This wave-field traverses a thin sample, to yield the complex disturbance $\psi(x, y, z = 0)$ over the plane $z = 0$, which then propagates through free space to the plane $z = \Delta z$. This plane forms the entrance surface of a given imaging device, which is capable of registering a series of intensity maps $I_1(x, y)$, $I_2(x, y)$, $I_3(x, y)$, etc., which correspond to states 1, 2, 3, etc., of the imaging system. Using phase retrieval techniques, the set of intensity maps $\{I_1, I_2, I_3, \ldots\}$ may be used to reconstruct the full complex wave-function $\psi_R \equiv \psi(x, y, z = 0)$ of the wave-field in the plane $z = 0$. Because this confers total knowledge of the coherent wave-field emerging from the sample, one can use ψ_R as input to a 'virtual optics' computer programme, which calculates the image $I(x, y, \boldsymbol{\tau})$, which would have been produced by an imaging system in the state completely characterized by the set $\tau = \{\tau_1, \tau_2, \ldots\}$ of real parameters $\tau_1, \tau_2, \ldots$

wavelengths are too high for existing detectors to be directly sensitive to the phase of the disturbance (Born & Wolf, 1993). Rather, existing detectors return signals that may be related to the modulus of the disturbance, with phase information being lost. The field of phase retrieval, which seeks to determine phase information from intensity measurements alone, is now sufficiently advanced for the input wave-functions mentioned earlier to be routinely inferred from measurement data in a wide variety of contexts (see, for example, Paganin & Nugent, 2001, and references therein).

This allows us to investigate the combination of phase retrieval, which yields the complex 'input' wave-function created by the interaction of coherent probe radiation with a sample of interest, with the use of virtual optics in which image-processing software forms an extension of the optical system (Lichte *et al.*, 1992, 1993; Yaroslavsky & Eden, 1996; Bajt *et al.*, 2000; Allman *et al.*, 2002; Barone-Nugent *et al.*, 2002). Once one has retrieved the phase of the input wave-function using the phase retrieval or phase-measurement method of choice, one has total knowledge of the information encoded in the said wave-field. This total knowledge is powerful, because it allows one to emulate the subsequent action of any imaging system for which an associated mathematical transform can be written, regardless of whether that system is realizable in hardware. Thus one can speak of an 'omni-microscope', which is able to emulate all possible modes of microscopy; the optical information processing of such a hybrid system is performed partly by optical hardware, and partly by optical software (Yaroslavsky & Eden, 1996; Brady & Rahman, 2002; Cathey & Dowski, 2002). Possible future applications of this methodology include coherent X-ray and atom imaging, in which expensive and/or difficult-to-fabricate mirrors or beam splitters may be realized using software rather than hardware.

To make these ideas more concrete, consider Fig. 1, which shows a generic piece of optical hardware ('physical imaging system') whose state may be changed so as to record a sufficient sequence of images to reconstruct the amplitude and phase of the coherent wave-function over a given plane downstream of the sample, with the said sample being illuminated by well-characterized coherent radiation from a given source (see, for example, Allen *et al.*, 2001; Paganin & Nugent, 2001; and Gureyev *et al.*, 2001, for examples of how such a phase retrieval is performed). The optical software, namely a 'virtual optics imaging system', is then able to use this knowledge of the wave-function to compute the image that would be

produced by any imaging system (Lichte *et al.*, 1993). The user can then choose from this infinite multiplicity of representations, adopting the imaging mode or modes best suited to a particular application.

We close this introduction with a brief overview of the remainder of the paper. Section 2 gives a mathematical introduction to the theory of hybrid physical–virtual imaging systems. This theory is broadly applicable to a range of imaging systems for which phase retrieval is possible. We then focus our attention on a model case in which the phase-retrieval step can be performed using a single defocused image of a single-material object, obtained using a point-projection X-ray microscope (Mayo *et al.*, 2002; Paganin *et al.*, 2002). Section 3 gives an experimental demonstration of these ideas: we use software to transform a point-projection microscope into what we term an 'omni-microscope', i.e. a hybrid virtual–physical microscope that is capable of an infinite variety of imaging modalities including Zernike phase contrast (Zernike, 1942), differential interference contrast (Nomarski & Weill, 1955), Schlieren imaging (Meyer-Arendt, 1992) and diffraction-enhanced imaging (Förster *et al.*, 1980; Somenkov *et al.*, 1991; Davis *et al.*, 1995; Ingal & Beliaevskaya, 1995; Chapman *et al.*, 1997). Section 4 gives a brief discussion, which includes consideration of the complexities involved in generalizing this work to partially coherent imaging systems. We conclude with section 5.

2. Theory

2.1. Operator theory of free-space diffraction

Figure 1 denotes a coherent scalar radiation wave-field that is created by a monochromatic source, before being elastically scattered by a sample of interest and then allowed to propagate through free space. Denote the complex disturbance of this wave-field by $\Psi(x, y, z, t) = \psi(x, y, z)\exp(i\omega t)$, where (x, y, z) denotes a Cartesian coordinate system with the x–y plane being perpendicular to the optic axis z, ω is the angular frequency, t is time, and ψ is the time-independent part of the full wavefunction Ψ. The harmonic time dependence $\exp(i\omega t)$ will henceforth be ignored. All sources and samples are assumed to lie in the half space $z < 0$, with $z > 0$ being free space.

The intensity $I(x, y, z) \equiv |\psi(x, y, z)|^2$ over any given plane $z > 0$ can be obtained from $\psi(x, y, z = 0)$ using the diffraction integral that solves the boundary value problem for the particular differential equation obeyed by the radiation wave-field. Operationally, this is denoted:

$$I(x, y, z) = \hat{M}\hat{D}(z)\,\psi(x, y, z = 0),\ z \geq 0, \tag{1}$$

where the diffraction operator $\hat{D}(z)$ acts on the (input) boundary value $\psi(x, y, z = 0)$ of the wavefunction to produce the (output) propagated wavefunction $\psi(x, y, z)$, and the operator $\hat{M}$ returns the modulus squared of the function on which it acts (i.e. $\hat{M}\psi \equiv |\psi|^2$).

2.2. Operator theory of optical imaging systems

The action of an arbitrary optical imaging system may also be viewed in terms of an operator acting on an input to yield an output. Consider an optical imaging system, the state of which is parameterized by the set $\tau\{\tau_1, \tau_2, \ldots\}$ of real numbers $\tau_1, \tau_2, \ldots$ Suppose that such an imaging system is placed in the half-space $z > 0$, leading to the formation of a given real image $I(x, y, \boldsymbol{\tau})$. The action of this optical system may be viewed in operational terms as:

$$I(x, y, \boldsymbol{\tau}) = \hat{M}\hat{D}(\boldsymbol{\tau})\,\psi(x, y, z = 0). \tag{2}$$

Here, the complex input wavefunction $\psi(x, y, z = 0)$ is acted upon by the operator $\hat{D}(\boldsymbol{\tau})$ characterizing the imaging system, to yield the wavefunction over the surface of the detector; the squared modulus of this quantity is the real output image $I(x, y, \boldsymbol{\tau})$.

As an example of the ideas sketched above, consider the radiation in Fig. 1 to consist of monochromatic scalar electromagnetic waves. These obey the Helmholtz equation $(\nabla^2 + k^2)\psi(x, y, z) = 0)$, where $k = 2\pi/\lambda$ and λ is the radiation wavelength (Nieto-Vesperinas, 1991). We restrict ourselves to such Helmholtz wave-fields for the remainder of the paper, although the formalism discussed here is applicable to a broader class of complex scalar wave-fields such as those that obey non-linear differential equations like the non-linear Schrödinger equation (Kivshar & Luther-Davies, 1998). Suppose, further, that there are no 'backward travelling' components to the Helmholtz wave-field in the half-space $z > 0$; more precisely, we assume that the elementary travelling plane waves, into which the disturbance in $z > 0$ may be decomposed via a Fourier integral, are such that the momentum vector of each plane wave component has a positive projection on the z-axis. Given this assumption, the boundary value problem of obtaining $\psi(x, y, z), z > 0$, from $\psi(x, y, z = 0)$, is solved by the angular spectrum representation of the Rayleigh–Sommerfeld diffraction integral of the first kind ('RS1'), which may be written using the notation of Eq. (1) as $I(x, y, z) = \hat{M}\hat{D}_{RS1}(z)\psi(x, y, z = 0)$, where (Montgomery, 1968, 1969; Saleh & Teich, 1991):

$$\hat{D}_{RS1}(z) = \hat{F}^{-1}\exp\left(iz\sqrt{k^2 - k_x^2 - k_y^2}\right)\hat{F}\,. \tag{3}$$

Here, the two-dimensional Fourier transform operator $\hat{F}$ and its inverse $\hat{F}^{-1}$ are defined using the convention given in Eq. (A6) of the appendix, and (k_x, k_y) are the Fourier coordinates conjugate to the real space coordinates (x, y). The operator in Eq. (3) is unitary if evanescent waves are neglected (Montgomery, 1981); note that Eq. (3) reduces to the Fourier representation of the Fresnel diffraction operator, if the binomial

approximation $(k^2 - k_x^2 - k_y^2)^{1/2} \approx k - (k_x^2 + k_y^2)/(2k)$ is made (Nazarathy & Shamir, 1980; Saleh & Teich, 1991).

To extend the above example, suppose the monochromatic scalar electromagnetic waves to be paraxial, and that a shift-invariant linear optical imaging system (Goodman, 1968) is placed in the half-space $z > 0$ (note that the system is linear at the level of wave-functions, but is non-linear at the level of intensity). The state of this imperfect imaging system is characterized by its 'transfer function' $T(k_x, k_y, \boldsymbol{\tau})$ (Goodman, 1968); the coefficients in the two-dimensional Taylor series expansion of the phase of this transfer function, if such an expansion exists, are closely related to the classical Seidel aberrations such as defocus, coma, astigmatism, etc. (Born & Wolf, 1993). Using the notation of Eq. (2), the action of our imaging system is then given by the following operator:

$$\hat{D}(\boldsymbol{\tau}) = \hat{F}^{-1} T(k_x, k_y, \boldsymbol{\tau}) \hat{F}. \tag{4}$$

Special cases of such 'aberrated' imaging systems include those that yield Zernike phase contrast, Schlieren phase contrast, inline holograms, differential interference contrast and diffraction-enhanced images. We briefly consider each of these in turn.

Zernike phase contrast. The Zernike phase contrast microscope renders colourless transparent samples visible by placing a phase-shifting glass plate in the back focal plane of an imaging system. In its simplest incarnation, this plate is of uniform thickness everywhere except along the optic axis, where a small transparent 'spot' retards the phase of the radiation by ϕ_0 radians (Zernike, 1942). To a good approximation, this system may be modelled using the following transfer function in Eq. (4):

$$T_{ZER}(k_x, k_y, \boldsymbol{\tau}) = \begin{cases} \exp(i\phi_0), k_x^2 + k_y^2 \le k_r^2, \\ 1, k_x^2 + k_y^2 > k_r^2, \end{cases} \quad \boldsymbol{\tau} = (\phi_0, k_r), \tag{5}$$

where k_r is proportional to the radius of the phase-retarding spot, and we have ignored an irrelevant constant additive phase factor, which is due to the constant phase shift of the glass in the plate.

Schlieren phase contrast. Schlieren phase contrast works by using a so-called 'knife edge', which is located in the back focal plane of an imaging system, passing through the optic axis (Meyer-Arendt, 1992). This knife edge has the effect of blocking the passage of half of the transverse spatial frequencies in the radiation wave field. Such an optical system is modelled by the transfer function:

$$T_{SCH}(k_x, k_y, \boldsymbol{\tau}) = \begin{cases} 0, k_y \ge k_x \tan\theta, \\ 1, k_y < k_x \tan\theta, \end{cases} \quad \boldsymbol{\tau} = \theta, \tag{6}$$

where θ is the angle that the knife edge makes with the positive k_x-axis, and θ increases as one winds about the origin $k_x = k_y = 0$ in an anticlockwise direction.

Inline holography. Inline holography, invented by Gabor (Gabor, 1948), propagates the wave-field $\psi(x, y, z = 0)$ through a distance z before recording the square modulus of the resulting disturbance. The relevant transfer function in Eq. (4) is:

$$T_{HOL}(k_x, k_y, \boldsymbol{\tau}) = \hat{F} \hat{D}_{RS1}(z) \hat{F}^{-1}$$

(see Eq. 3).

Differential interference contrast. In its simplest form, differential interference contrast takes a coherent wave-field of interest, say $\psi(x, y, z = 0)$, and then interferes this wave-field with a copy of itself that has been given both (i) a slight transverse displacement $(\Delta x, \Delta y)$ and (b) a phase shift ϕ_0 (Nomarski & Weill, 1955). Thus the intensity of the resulting wave-field is $|\psi(x, y, z = 0) + \exp(i\phi_0)\psi(x - \Delta x, y - \Delta y, z - \Delta z = 0)|^2$, from which one can readily show (using the Fourier shift theorem) that the transfer function in Eq. (4) becomes:

$$T_{DIC}(k_x, k_y, \boldsymbol{\tau}) = 1 + \exp(i(\phi_0 - k_x \Delta x - k_y \Delta y)), \quad \boldsymbol{\tau} = (\phi_0, \Delta x, \Delta y). \tag{7}$$

Diffraction-enhanced imaging. In diffraction-enhanced imaging (DEI) (Förster *et al.*, 1980; Somenkov *et al.*, 1991; Davis *et al.*, 1995; Ingal & Beliaevskaya, 1995; Chapman *et al.*, 1997), the wave-field of interest impinges on a perfect crystal, which is set in a position near a certain Bragg or Laue reflection with respect to the average wave vector $\boldsymbol{k}$ of the incident wave-field. The process of diffraction in the crystal affects the part of the spatial Fourier spectrum of the incident wave that lies in the diffraction plane. Mathematically, the intensity of the wave emerging from the crystal can be described in the case of two-beam Bragg reflection by Eq. (4) with (see, for example, Nesterets & Punegov, 2000):

$$T_{DEI}(k_x, k_y, \boldsymbol{\tau}) = \begin{cases} \sigma_h/\xi_2, & \text{if } \mathrm{Im}(\xi) > 0, \\ \sigma_h/\xi_1, & \text{if } \mathrm{Im}(\xi) \le 0, \end{cases} \quad \boldsymbol{\tau} = (\lambda, \theta_B, \Delta\theta, b, \chi_0, \chi_{\pm h}, C), \tag{8a}$$

where θ_B is the Bragg angle, $\Delta\theta$ is the deviation of the crystal from the exact Bragg position, χ_0 and $\chi_{\pm h}$ are the Fourier coefficients of the crystal polarizability, $b = \lambda_0/\lambda_h$ is the asymmetry factor, $\gamma_{0,h} = \sin\theta_{1,2}$ are the sines of the angle between the crystal surface and the incident and reflected beams, respectively, $C = 1$ for σ-polarization and $C = \cos(2\theta_B)$ for π-polarization, and:

$$\xi_{1,2} = (-\eta \pm \xi)/2, \tag{8b}$$

$$\eta = \pi/(\lambda\gamma_0)[(1 + b)\chi_0 + 2b\Delta\theta \sin(2\theta_B)], \tag{8c}$$

$$\xi = \sqrt{\eta^2 - 4\sigma_h\sigma_{-h}}\,, \tag{8d}$$

$$\sigma_{\pm h} = \frac{\pi\chi_{\pm h}C}{\lambda\gamma_{h,0}}, \tag{8e}$$

$$\Delta\theta = k\gamma_0 k_x. \tag{8f}$$

The above examples of shift-invariant linear imaging systems are now supplemented with two further systems that are neither shift-invariant nor linear: interferometers and off-axis holography. The concept of a transfer function is not meaningful for such systems, and we must therefore work with Eq. (2) rather than Eq. (4).

Interferometry. Interferograms are obtained by adding a reference plane wave $\alpha\exp(i(k_x^0x + k_y^0y + \beta))$ to the complex disturbance $\psi(x, y, z = 0)$, and then recording the intensity (i.e. modulus squared) of the resulting wave-field:

$$I_{INT}(x, y, \boldsymbol{\tau}) = \hat{M}(\psi(x, y, z = 0) + \alpha\exp(i(k_x^0x + k_y^0y + \beta))),\quad \boldsymbol{\tau} = (\alpha, \beta, k_x^0, k_y^0). \tag{9}$$

Here, α is the amplitude of the reference plane wave, β is a spatially uniform phase shift, and (k_x^0, k_y^0) specifies the tilt of the reference wave with respect to the (x, y)-plane.

Off-axis holography. Off-axis holograms are obtained by interference of a tilted plane wave with the wave transmitted by a sample, after the latter wave has been allowed to propagate through free space (Born & Wolf, 1993). The intensity of the resulting off-axis hologram is therefore:

$$I_{OAH}(x, y, \boldsymbol{\tau}) = \hat{M}(\hat{D}_{RS1}(z)\psi(x, y, z = 0) + \alpha\exp(i(k_x^0x + k_y^0y + \beta))),\quad \boldsymbol{\tau} = (\alpha, \beta, k_x^0, k_y^0, z), \tag{10}$$

where all symbols are as previously defined.

2.3. Phase retrieval, phase measurement and wave-function reconstruction

The phase problem, in an imaging context, can be broadly stated as follows: given a series $\{I_1(x, y), I_2(x, y), \ldots\}$ of one or more two-dimensional intensity maps produced by a given imaging system (in states $\boldsymbol{\tau}_1, \boldsymbol{\tau}_2, \ldots$, respectively) with a fixed two-dimensional complex scalar wave-field $\psi(x, y, z = 0)$ as unknown input, can one reconstruct $\psi(x, y, z = 0)$? We will not review the many successful approaches to this question (see, for example, Luke *et al.*, 2002), examples of which include methods based on phase-stepped interferometry (Younus & Alam, 1999), the transport-of-intensity equation (Teague, 1983; Gureyev *et al.*, 2001; Paganin & Nugent, 2001) and generalized forms of the Gerchberg–Saxton algorithm (Gerchberg & Saxton, 1972; Fienup, 1982; Allen *et al.*, 2001). In the present rather general context, the salient point is that, for all of these methods, the reconstruction of the complex wavefunction $\psi(x, y, z = 0)$ given $\{I_1, I_2, \ldots; \boldsymbol{\tau}_1, \boldsymbol{\tau}_2, \ldots\}$ as input data can be formally written as:

$$\psi(x, y, z = 0) = \hat{R}\{I_1(x, y), I_2(x, y), \ldots; \boldsymbol{\tau}_1, \boldsymbol{\tau}_2, \ldots\}. \tag{11}$$

Here, the 'wave-field reconstruction operator' $\hat{R}$ is dependent on the phase measurement or phase retrieval method being employed; the said operator acts on the set $\{I_1, I_2, \ldots; \boldsymbol{\tau}_1, \boldsymbol{\tau}_2, \ldots\}$ to yield $\psi(x, y, z = 0)$.

2.4. Omni optics

Consider, again, the scenario shown in Fig. 1. Well-characterized coherent scalar radiation from a given source passes through a sample of interest, leading to the formation of a complex wave-function $\psi(x, y, z = 0)$ over the plane $z = 0$. This wavefunction then propagates through free space to the plane $z = \Delta z$. This plane forms the entrance surface of a given imaging device, which is capable of registering a series of two-dimensional intensity maps $\{I_1(x, y), I_2(x, y), \ldots\}$ that correspond to states $\{\boldsymbol{\tau}_1, \boldsymbol{\tau}_2, \ldots\}$ of the imaging system. Using phase retrieval techniques, the set of intensity maps $\{I_1, I_2, I_3, \ldots\}$ may be used to reconstruct the full complex wave-function $\psi_R \equiv \psi(x, y, z = 0)$ of the wave-field in the plane $z = 0$, a process which is formally represented by Eq. (11). Because it confers total knowledge of the coherent wave-field emerging from the sample, one can use ψ_R as input to a 'virtual optics' computer programme which numerically implements Eq. (2), to calculate the image $I(x, y, \boldsymbol{\tau})$, which would have been produced by an imaging system in the state completely characterized by the set $\boldsymbol{\tau} \equiv \{\tau_1, \tau_2, \ldots\}$ of real parameters $\tau_1, \tau_2, \ldots$

The above two-step procedure, namely wave-function reconstruction followed by image processing using virtual optics, is summarized in:

$$I(x, y, \boldsymbol{\tau}) = \hat{M}\hat{D}(\boldsymbol{\tau})\hat{R}\{I_1(x, y), I_2(x, y), \ldots; \boldsymbol{\tau}_1, \boldsymbol{\tau}_2, \ldots\}, \tag{12}$$

where all symbols are as defined previously (cf. Gabor, 1948). Hybrid physical–virtual optical systems described by Eq. (12) are termed 'omni optics', because of their ability to emulate the action of an infinite variety of optical imaging systems. The 'software lens' component of an omni-optical system is not restricted to the emulation of existing optical systems: one can emulate optics that are not realizable using existing technology (Cathey & Dowski, 2002; Peng, Yu & Cai, 2002). For example, one could synthesize a 'broad bandpass' DEI set-up with an arbitrary crystal transfer function $T_{DEI}(k_x, k_y, \boldsymbol{\tau})$, which is not restricted by available crystals.

2.5. Example: X-ray omni microscopy

We now give an example of the application of these ideas, by

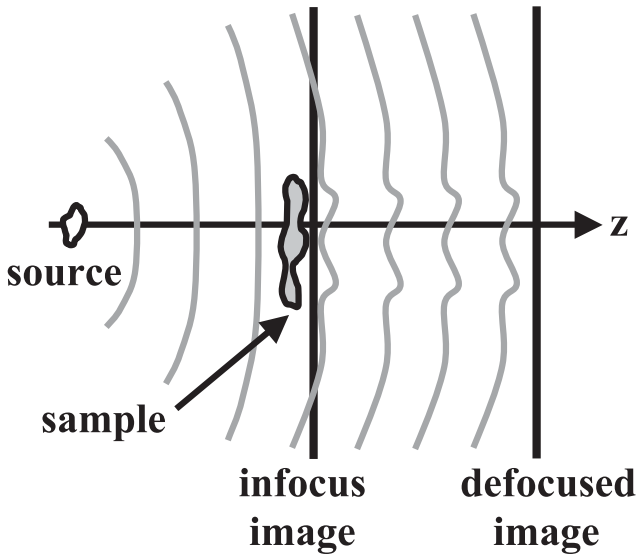

Fig. 2. Sketch of the point-projection X-ray microscope geometry. Here, R_1 is the source-to-sample distance, and R_2 is the sample-to-detector distance.

showing how a lensless X-ray point projection microscope can, when equipped with the requisite software, emulate an infinite variety of optical imaging systems, including those that yield interferograms, Zernike phase contrast, Schlieren imaging, diffraction-enhanced imaging, differential interference contrast and inline holograms (cf. Allman *et al.*, 2002; Barone-Nugent *et al.*, 2002). An experimental demonstration for the same system, using both laboratory and synchrotron radiation sources, will be given in the following section.

Consider a point source of polychromatic scalar X-ray radiation, which passes through a sample of interest before propagating through free space and then falling on the surface of an imaging detector (see Fig. 2). Importantly, the intensity registered by the detector is a function of both the amplitude and the phase changes imprinted on the probe radiation upon passage through the sample; this phenomenon of 'X-ray phase contrast' has been discussed by many authors (see Wilkins *et al.*, 1996, and references therein). As shown by Mayo *et al.* (2002), the detector is able to filter out a single quasi-monochromatic component of the polychromatic radiation that falls on its surface, to yield the phase contrast image that would have been produced if the point source were quasi-monochromatic (cf. Wilkins *et al.*, 1997; Gureyev, 1999).

Suppose the sample to comprise a single material of known refractive index $n \equiv 1 - \delta$ and absorption coefficient μ. The sample is assumed to be sufficiently thin to ensure the validity of the projection approximation given by Eq. (A8) in the appendix. The quasi-monochromatic component of the wave-field downstream of the sample is assumed to be sufficiently weakly expanding that its spatial evolution is governed by the parabolic Eq. (A1). Because we are imaging with a point source, the image $I(x, y, z = \Delta z)$ will have a magnification of $M = (\Delta z + R_1)/R_1$, where R_1 is the distance from the source to the sample and Δz is the distance from the sample to the detector. For this case, the wave-field reconstruction operator appearing in Eq. (11) is given by solving the relevant transport-of-intensity equation (Teague, 1983; see also Eq. A2), to yield the following formal solution:

$$\hat{R}\{I(x, y, z = \Delta z), \boldsymbol{\tau} = (k, \mu, \delta, \Delta z, I_0, M)\} = I_0^{-ik\delta/\mu} \exp(i\phi_0) \left(\frac{M^2}{1 - \mu^{-1} M^{-1} \delta \Delta z \nabla_\perp^2} I(Mx, My, z = \Delta z) \right)^{\frac{1}{2} + ik\delta/\mu} . \quad (13)$$

Here, I_0 is the intensity (considered to be approximately uniform) of the incident spherical wave over the region of interest, ϕ_0 is an irrelevant unknown constant phase shift, and $\nabla_\perp^2 \equiv \partial^2/\partial x^2 + \partial^2/\partial y^2$ denotes the Laplacian in the x–y plane. See the appendix for a derivation of this formal expression, together with a means for evaluating it using the fast Fourier transformation.

Using Eq. (13) for the wave-function reconstruction operator $\hat{R}$ (cf. Eq. 11), one can reconstruct the complex wave-function $\psi(x, y, z = 0)$, which existed in the plane $z = 0$; one can then use Eq. (12) to compute the image that would have been produced by an arbitrary imaging system. This two-fold imaging process, namely hardware imaging, followed by phase retrieval plus software emulation of an optical system, gives an example of the general process denoted by Eq. (12).

3. Experimental examples

In this section we present some experimental examples illustrating the theory described above. For the first example we used a portion of an in-line X-ray image collected at beamline ID22 of the European Synchrotron Radiation Facility. The sample was an approximately 100 μm thick section of dried human femur bone. The image was obtained using plane highly monochromatic X-ray waves with wavelength $\lambda = 0.62$ Å ($E = 20$ keV), and an object-to-detector distance of $\Delta z = 20$ cm. The detector system for high-resolution microradiography at ID22 (Weitkamp *et al.*, 1999) was used, with an effective pixel size of 0.33 μm. Figure 3(a) presents a 2048×2048-pixel subimage of the raw data, with dimensions 676×676 μm in the object plane. A 200-μm scale bar has been included in this image, with all other images in this figure corresponding to the same magnification. This image clearly shows cross-sections of haversian canals, osteocytes and other features. Owing to the large object-to-detector distance phase-contrast features are visible in the image. These features can be seen primarily in the sharp black and white fringes near the edges of the holes in the bone. This appearance is typical for X-ray in-line phase contrast in the near field (Snigirev *et al.*, 1995; Wilkins *et al.*, 1996).

As the dried bone can be considered to consist predominantly of a single material (apatite), we were able to apply

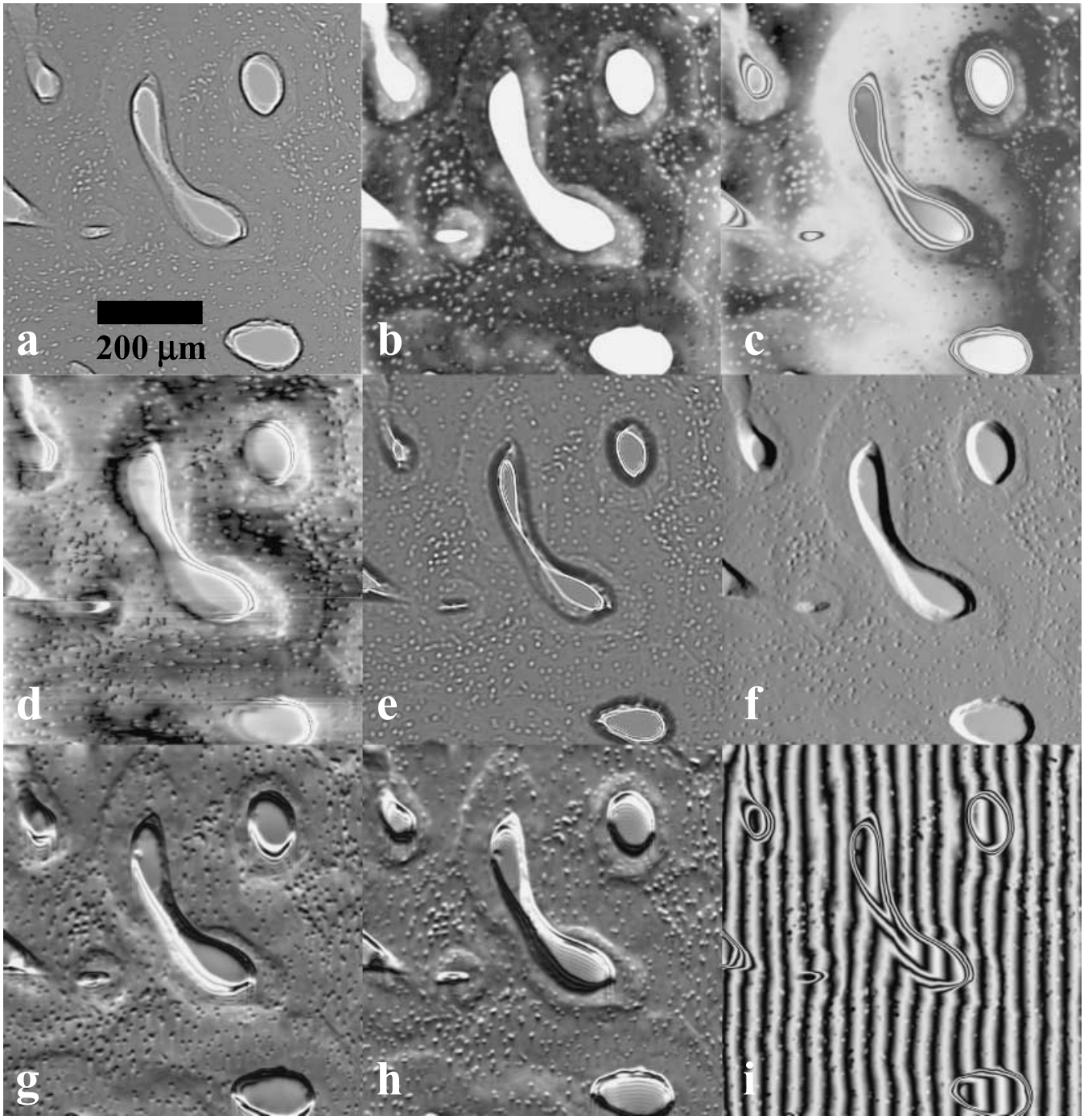

Fig. 3. X-ray omni microscopy of dried human femur bone. (a) X-ray propagation-based phase-contrast radiograph of dried human femur; (b) recovered projected thickness $T(x, y)$ of apatite, obtained by applying Eqs (A8a) and (A9) to the data in (a); (c) simulated Zernike phase-contrast image obtained using Eq. (5) with $\phi_0 = \pi$ and $k_r = 10^{-3}\,\mu\text{m}^{-1}$; (d) simulated Schlieren image obtained using Eq. (6) with $\theta = \pi/2$; (e) simulated in-line hologram corresponding to a propagation distance of $z = 1$ m in Eq. (3); (f) simulated DIC image obtained using Eq. (7) with $\phi_0 = \pi$, $\Delta x = 0.33\,\mu$m and $\Delta y = 0$; (g) simulated DEI image using a symmetrical (111) Bragg reflection from a perfect Si crystal in the y–z plane (Eq. 8), with $\Delta\theta = 1.5''$; (h) as (g), but with $\Delta\theta = -1.5''$; (i) simulated interferogram (see Eq. 9) with $\alpha = 1$, $\beta = \pi$, $k_x^0 \cong 1.75\,\mu$m and $k_y^0 = 0$.

Eq. (13) for phase retrieval. We calculated the complex refractive index, $n = 1 - \delta + i\beta$, of apatite at $\lambda = 0.62$ Å to have $\delta = 1.66 \times 10^{-6}$ and $\beta = 9.62 \times 10^{-9}$ (note that $\beta = \lambda\mu/(4\pi)$). With these values of δ and β, we applied Eqs. (11) and (13) to the data in Fig. 3(a), so as to retrieve the input wave-function $\psi(x, y, z = 0)$. By the Beer–Lambert law of absorption, this retrieved field is easily related to the distribution $T(x, y)$ of the projected thickness of apatite along the direction of X-rays, via $|\psi(x, y, z = 0)|^2 = I_0 \exp(-\mu T(x, y))$; here, I_0 is the uniform intensity of the input probe beam over the object plane. Hence we were able to reconstruct $T(x, y)$, leading to the result shown in Fig. 3(b). The maximum of the reconstructed projected thickness of apatite was equal to approximately 90 μm, which was not inconsistent with the known thickness of the sample. Further, the reconstructed wave-function $\psi(x, y, z = 0)$ allowed us to simulate various phase-contrast microscopy modes, as described in the previous section. Figure 3(c) presents a simulated Zernike phase-contrast image obtained in accordance with Eq. (5), using $\phi_0 = \pi$ and $k_r = 10^{-3}$ μm^{-1}. Figure 3(d) is a simulated Schlieren phase-contrast image obtained using Eq. (6) with $\theta = \pi/2$. Figure 3(e) shows a calculated in-line hologram corresponding to the propagation distance $z = 1$ m (see Eq. 3). One can notice multiple Fresnel diffraction fringes near the edges (regions of abrupt density variations) in Fig. 3(e) that appeared due to the long object-to-detector distance. A simulated differential interference contrast image, obtained according to Eq. (7) with $\phi_0 = \pi$, $\Delta x = 0.33$ μm and $\Delta y = 0$, is presented in Fig. 3(f). This image strongly highlights density variations in the x direction. Next we calculated the DEI images using a simulated symmetrical (111) Bragg reflection from a perfect Si crystal in the y–z plane (Eq. 8). Only a narrow band of spatial Fourier frequencies around zero are transmitted by the DEI transfer function. Figure 3(g,h) show the DEI images at $\Delta\theta = 1.5''$ and $\Delta\theta = -1.5''$ positions, respectively, i.e. at symmetrical positions on either side of the exact Bragg position on the crystal rocking curve (cf. Chapman *et al.*, 1997). Typical one-sided oscillations of the DEI point-spread function can be seen extending down from edges in these images. The expected contrast reversal (Davis *et al.*, 1995) can be seen in Fig. 3(g,h). Finally, Fig. 3(i) shows a simulated interferogram (Eq. 9) with $\alpha = 1$, $\beta = \pi$, $k_x^0 \cong 1.75$ μm and $k_y^0 = 0$.

For the next example we used an image collected using an X-ray ultramicroscope based around an FEI XL-30 SFEG SEM (Mayo *et al.*, 2002). The sample was a common dust mite. The image was obtained using polychromatic divergent X-rays with the X-ray source size of approximately 0.2 μm created by focusing 15-kV electrons on a thin Ta target. The source-to-object distance was 4.3 mm and the object-to-detector distance was 254.7 mm, leading to an X-ray magnification of $M = 60.2$ and an effective defocus distance of $\Delta z/M = 4.2$ mm. The detector pixel size was 13 μm on the CCD, which was equivalent to 0.22 μm at the object plane. Figure 4(a) shows a 1024×1024-pixel subimage of the original XUM image of the dust mite, with dimensions 221×221 μm in the object plane. A 50-μm scale bar has been included in this image, with all other images in this figure corresponding to the same magnification. Again, owing to the large defocus distance we were able to register in-line phase-contrast effects in the form of black and white fringes near the edges of various sample features. The gradient in the background intensity distribution in the image was due to the curvature of the substrate used to support the dust mite on the sample stage.

In order to retrieve the phase by the method of Eq. (13) we had to use the simplifying assumption that the sample consisted predominantly of a single material (chitin). The polychromaticity of the X-ray radiation was handled by using an 'equivalent' median X-ray wavelength (Nugent *et al.*, 2001) of $\lambda = 2.5$ Å ($E = 5$ keV). As, unlike the situation considered in the first example, the above two assumptions may not be quantitatively accurate, the subsequent simulated images should be considered as qualitative only. If quantitative microscopy is required, then monochromatization by the XUM detector can be used (Gureyev *et al.*, 2001; Mayo *et al.*, 2002), and two or three images may be collected at different defocus distances or at different monochromatic wavelengths. Using such multiple images it is possible to reconstruct the distributions of the object plane intensity and phase even for samples consisting of multiple components with different X-ray transmission and refraction properties (Gureyev *et al.*, 2001; Mayo *et al.*, 2002).

Figure 4(b) presents the reconstructed distribution of the projected thickness in the sample obtained using the assumptions described above. We used this reconstructed projected thickness to calculate the distribution of phase and intensity in the object plane, and to simulate various phase-contrast microscopy modes described in the previous section. Figure 4(c) presents a simulated Zernike phase-contrast image obtained in accordance with Eq. (5) with $\phi_0 = \pi$ and $k_r = 4.5 \times 10^{-3}$ μm^{-1}. Note that the fringes in the upper region of the image are caused by the phase variations exceeding 2π, owing to the curved mylar film used to support the sample. The next image, Fig. 4(d), shows a simulated Schlieren phase-contrast mode corresponding to Eq. (6) with $\theta = \pi/2$. An in-line hologram corresponding to the simulated defocus distance $\Delta z/M = 4$ cm is presented in Fig. 4(e). Multiple Fresnel fringes near the edges and small features are clearly visible. Figure 4(f) shows a differential interference contrast image simulated in accordance with Eq. (7) using the following parameters: $\phi_0 = \pi$, $\Delta x = 0$ and $\Delta y = 0.22$ μm. Because the shift direction was vertical, features running in the horizontal direction are visible with high contrast in this last image. We also simulated several DEI images using symmetrical (111) Bragg reflection from a perfect Si crystal; at $\lambda = 2.5$ Å the rocking curve width was ~11.9″. DEI images were calculated, corresponding to the symmetrical positions $\Delta\theta = 6''$ and $\Delta\theta = -6''$ on either side of the rocking curve (data not shown). Figure 4(g,h) and show the sum and difference, respectively, of

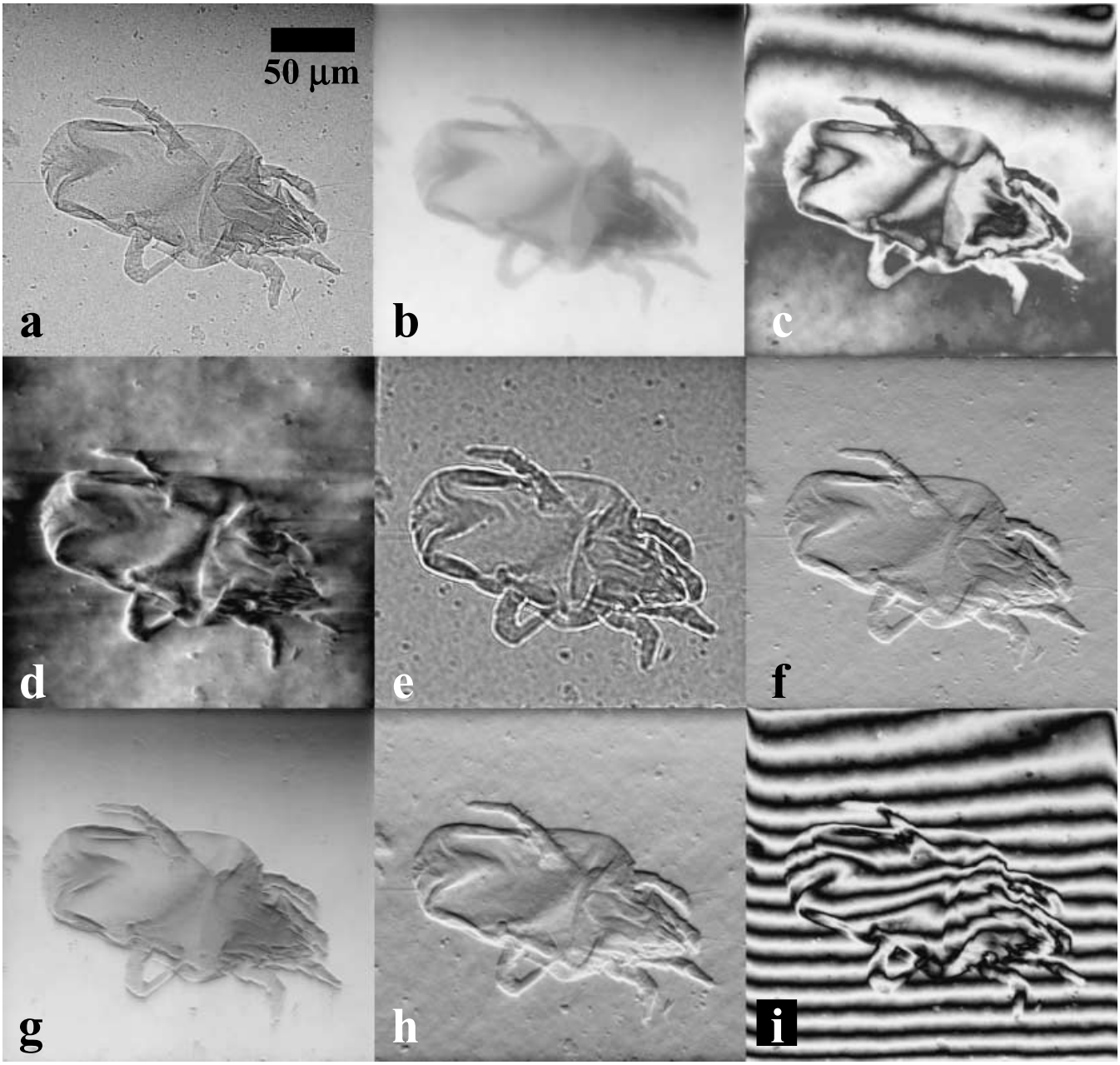

Fig. 4. X-ray omni microscopy of a common dust mite. (a) Point-projection X-ray micrograph of dust mite; (b) recovered projected thickness $T(x,y)$ of chitin, obtained by applying Eqs (A8a) and (A9) to the data in (a); (c) simulated Zernike phase-contrast image obtained using (5) with $\phi_0 = \pi$ and $k_r = 4.5 \times 10^{-3}$ μm^{-1}; (d) simulated Schlieren image obtained using Eq. (6) with $\theta = \pi/2$; (e) simulated in-line hologram corresponding to a propagation distance of $\Delta z/M = 4$ cm in Eq. (3); (f) simulated DIC image obtained using Eq. (7) with $\phi_0 = \pi$, $\Delta x = 0$ and $\Delta y = 0.22$ μm; (g) sum of simulated DEI images obtained using symmetrical (111) Bragg reflection from a perfect Si crystal, corresponding to the symmetrical positions $\Delta\theta = 6''$ and $\Delta\theta = -6''$ on either side of the rocking curve; (h) difference of the two DEI images mentioned in (g); (i) simulated interferogram (see Eq. 9) with $\alpha = 1$, $\beta = \pi$, $k_x^0 = 0$ and $k_y^0 \cong 2.5$ μm^{-1}.

these DEI images. This pair of figures may be compared with the theory of Chapman *et al.* (1997), which, subject to the geometrical optics approximation upon which their calculations are based, predicts that Fig. 4(g) should primarily reflect absorption contrast, whereas Fig. 4(h) should primarily display variations of the X-ray phase gradient. Finally, Fig. 4(i) shows a simulated interferogram (Eq. 9) with $\alpha = 1$, $\beta = \pi$, $k_x^0 = 0$ and $k_y^0 \cong 2.5$ μm^{-1}.

4. Discussion

Notwithstanding the success of the preceding applications of omni-microscopy, one may object that the associated analysis assumes ideal coherent imaging, thereby neglecting the effects of partially coherent illumination together with other factors associated with realistic imaging systems such as finite source size, noise, scatter, detector spectral efficiency, finite pixel size, etc. Here, we briefly discuss some of these issues, while leaving a fuller development of the same to a future work.

Let us begin with the question of partial coherence. As shown by Gureyev (1999), each monochromatic component of a paraxial optical wave-field in an arbitrary state of coherence obeys the same paraxial equation as listed in Eq. (A1) of the appendix; this is a consequence of the fact that each monochromatic component of a given partially coherent field is completely spatially and temporally coherent. For each of these monochromatic components, the associated transport of intensity equation is mathematically identical in form to Eq. (A2), with intensity replaced by spectral density. Therefore, in the context of omni microscopy, one may work with partially coherent radiation provided that one has a means of filtering out a given monochromatic component of the radiation striking the detector. Successful examples of phase retrieval in such a context have recently been demonstrated, using both the single-image phase retrieval algorithm described in the appendix (Mayo *et al.*, 2002; Paganin *et al.*, 2002) and a three-image phase retrieval algorithm that discards the assumption of a single-material object and takes, as input data, three defocused images over a given plane, which are obtained by filtering out three different monochromatic components of the radiation striking the detector (Gureyev & Wilkins, 1998; Gureyev *et al.*, 2001; Mayo *et al.*, 2002). Phase retrieval is also possible using unfiltered polychromatic radiation (Wilkins *et al.*, 1996; Paganin & Nugent, 1998; Gureyev, 1999; Nugent *et al.*, 2001; McMahon *et al.*, 2003); therefore, in what amounts to a special case of the fully polychromatic scenario, phase retrieval is possible using quasi-monochromatic radiation of insufficient coherence for interferometric phase determination (e.g. Barty *et al.*, 1998).

In all of the above contexts regarding phase retrieval using partially coherent radiation, it is sometimes possible – subject, of course, to the relevant approximations – to reconstruct the projected thickness of each element in the sample. As an example, consider the analysis of Gureyev *et al.* (2002); although they considered imaging using rather coherent X-ray radiation from a third-generation synchrotron source, their formalism may be applied without modification to energy-filtered monochromatic images obtained using partially coherent radiation. This analysis, which implemented a method for recovering the projected thickness of a sample composed of two distinct materials given defocused images obtained over the same plane but corresponding to three different monochromatic components of the wave-field, can be generalized to the case of a sample that consists of N different materials (Gureyev *et al.*, 2002). We cite this example for the following reason: if one can reconstruct the projected thickness of each material present in the sample, using image data obtained while illuminating the said sample with partially coherent radiation, then this knowledge of the sample can be used to emulate in software the action of any partially coherent imaging system on that sample, provided that: (i) one knows the wavelength dependence of the complex refractive index of each material in the sample; (ii) the projection approximation is valid for the imaging system one wishes to emulate; and (iii) one can neglect, for the purposes of emulation, the effects resulting from fine structural details in the sample that were not resolved in the original reconstruction. The emulated image can, subject to the approximations already listed, also take into account the effects of scatter, finite detector resolution, blurring owing to source size, etc. Regarding the integral transforms describing image formation when these complicating factors are taken into account: these transforms can always be written down, in principle, using the constructive methods of mathematics, given an appropriate model for the optics, the detector and the interaction of the radiation with the reconstructed sample. Such a methodology may perhaps be of some use as a stringent test of the principles of omni microscopy, because it will permit a direct comparison of the results obtained using an omni-microscope, with the results of realistic imaging systems that use hardware rather than software for the realization of a given imaging mode.

In the interests of simplicity, this paper has not considered the emulation of partially coherent imaging systems, choosing instead to simulate what one would measure if we had monochromatic radiation in a given emulated imaging mode such as DEI, DIC, Zernike phase contrast, etc. The effects of partial coherence in both the hardware optics and the software optics may be overcome using the methods described earlier. Within the context of the single-material object approximation outlined in the appendix, it is clear that once the projected thickness of a given sample has been determined, the emulation of partially coherent imaging systems is readily implemented: one need only take a theory of partially coherent image formation with the requisite level of sophistication, and thence calculate the image that would be obtained of a sample composed of the given material and with the measured distribution of projected thickness.

If one wishes to go beyond the single-material approximation, then one can in principle reconstruct the complex amplitude of each monochromatic component of the radiation in the object plane, by performing a phase reconstruction at every wavelength. Such an approach would have the advantage of not making any strong assumptions about the sample, and would merely demand that the polychromatic radiation emerging from that sample should be paraxial. The large amount of data that must be taken in such an approach can

be greatly reduced by certain *a priori* knowledge about the sample, as argued in the preceding paragraphs. Thus, if one reconstructs the projected thickness of every material in a given sample by applying one of the appropriate methods of phase retrieval (e.g. that of Gureyev *et al.*, 2002), then one can calculate each monochromatic component of the object-plane polychromatic field that would result if the sample were illuminated with a given partially coherent wave-field. One would then have a complete description of the wave-field in the polychromatic case, permitting emulation of the subsequent action of an arbitrary imaging system.

5. Conclusion

A formalism was obtained for describing hybrid virtual–physical imaging systems, which we term 'omni optics' because of their infinite flexibility. In such systems, image formation proceeds in two stages: reconstruction of the complex amplitude of a scalar field over a given plane, followed by digital processing to emulate the action of an arbitrary optical imaging system. We gave an experimental demonstration by showing that a lensless X-ray point projection microscope can, when augmented with appropriate software, emulate an infinite variety of optical imaging systems including those that yield interferograms, Zernike phase contrast, Schlieren imaging and diffraction-enhanced imaging. The effects of partial coherence, noise, scatter, detector resolution, etc., were briefly discussed in the context of both hardware and software optics, but we shall leave to a future publication a more detailed consideration of these issues.

Acknowledgements

We acknowledge partial support by a grant from the 'Access to Major Research Facilities Program' managed by the Australian Nuclear Science and Technology Organization. We also acknowledge support from the Australian Synchrotron Research Program (ASRP), which is funded by the Commonwealth of Australia under the Major National Research Facilities Program. We acknowledge encouragement by XRT Limited for this research. We are grateful to Prof J. G. Clement, Dr S. Feik and Dr S. O'Connell for permission to use the bone sample from the Melbourne Femur Collection housed at the School of Dental Science, University of Melbourne. Andrew Pogany and Chris Rossouw provided a number of insightful comments, which led to an improved manuscript.

References

Allen, L.J., Oxley, M.P. & Paganin, D. (2001) Computational aberration correction for an arbitrary linear imaging system. *Phys. Rev. Lett.* **87**, Art. no. 123902.

Allman, B.E., Nassis, L., von Bibra, M.L., Bellair, C.J., Kabbara, A., Barone-Nugent, E., Gaeth, A.P., Delbridge, L.M. & Nugent, K.A. (2002) Optical phase microscopy: quantitative imaging and conventional phase analogs. *Microsc. Anal.*, **25**, 5–7.

Bajt, S., Barty, A., Nugent, K.A., McCartney, M., Wall, M. & Paganin, D. (2000) Quantitative phase-sensitive imaging in a transmission electron microscope. *Ultramicroscopy*, **83**, 67–73.

Barone-Nugent, E.D., Barty, A. & Nugent, K.A. (2002) Quantitative phase-amplitude microscopy I: optical microscopy. *J. Microsc.* **206**, 194–203.

Barty, A., Nugent, K.A., Paganin, D. & Roberts, A. (1998) Quantitative optical phase microscopy. *Opt. Lett.* **23**, 817–819.

Born, M. & Wolf, E. (1993) *Principles of Optics*, 6th corrected edition. Pergamon Press, Oxford, pp. 211–213, 457, 493.

Brady, D.J. & Rahman, Z. (2002) Integrated analysis and design of analog and digital processing in imaging systems: introduction to the feature issue. *Appl. Opt.* **41**, 6049.

Cathey, W.T. & Dowski, E.R. (2002) New paradigm for imaging systems. *Appl. Opt.* **41**, 6080–6092.

Chapman, D., Thomlinson, W., Johnston, R.E., Washburn, D., Pisano, E., Gmür, N., Zhong, Z., Menk, R., Arfelli, F. & Sayers, D. (1997) Diffraction enhanced X-ray imaging. *Phys. Med. Biol.* **42**, 2015–2025.

Cowley, J.M. (1981) *Diffraction Physics*, 2nd revised edition. North-Holland, Amsterdam.

Davis, T.J., Gao, D., Gureyev, T.E., Stevenson, A.W. & Wilkins, S.W. (1995) Phase contrast imaging of weakly absorbing materials using hard X-rays. *Nature*, **373**, 595–598.

Fienup, J.R. (1982) Phase retrieval algorithms: a comparison. *Appl. Opt.* **21**, 2758–2769.

Förster, E., Goetz, K. & Zaumseil, P. (1980) Double crystal diffractometry for the characterization of targets for laser fusion experiments. *Kristall Technik*, **15**, 937–945.

Gabor, D. (1948) A new microscopic principle. *Nature*, **161**, 777–778.

Gerchberg, R.W. & Saxton, W.O. (1972) A practical algorithm for the determination of phase from image and diffraction plane pictures. *Optik*, **35**, 237–246.

Goodman, J.W. (1968) *Introduction to Fourier Optics*. McGraw-Hill, San Francisco.

Gureyev, T.E. (1999) Transport of intensity equation for beams in an arbitrary state of temporal and spatial coherence. *Optik*, **110**, 263–266.

Gureyev, T.E., Mayo, S., Wilkins, S.W., Paganin, D. & Stevenson, A.W. (2001) Quantitative in-line phase-contrast imaging with multienergy X rays. *Phys. Rev. Lett.* **86**, 5827–5830.

Gureyev, T.E., Stevenson, A.W., Paganin, D.M., Weitkamp, T., Snigirev, A., Snigireva, I. & Wilkins, S.W. (2002) Quantitative analysis of two-component samples using in-line hard X-ray images. *J. Synchrotron Rad.* **9**, 148–153.

Gureyev, T.E. & Wilkins, S.W. (1998) On X-ray phase retrieval from polychromatic images. *Opt. Comm.* **147**, 229–232.

Ingal, V.N. & Beliaevskaya, E.A. (1995) X-ray plane-wave topography observation of the phase contrast from a non-crystalline object. *J. Phys. D. Appl. Phys.* **28**, 2314–2317.

Kivshar, Y.S. & Luther-Davies, B. (1998) Dark optical solitons: physics and applications. *Phys. Reports*, **298**, 81–197.

Lichte, H., Kessler, P., Lenz, D. & Rau, W.-D. (1993) 0.1 nm information limit with the CM30FEG-Special Tübingen. *Ultramicroscopy*, **52**, 575–580.

Lichte, H., Völkl, E. & Scheerschmidt, K. (1992) First steps of high resolution electron holography into materials science. *Ultramicroscopy*, **47**, 231–240.

Luke, D.R., Burke, J.V. & Lyon, R.G. (2002) Optical wavefront reconstruction: theory and numerical methods. *SIAM Rev.* **44**, 169–224.

Mayo, S.C., Miller, P.R., Wilkins, S.W., Davis, T.J., Gao, D., Gureyev, T.E., Paganin, D., Parry, D., Pogany, A. & Stevenson, A.W. (2002) Quantitative X-ray projection microscopy: phase-contrast and multi-spectral imaging. *J. Microsc.* **207**, 79–96.

McMahon, P.J., Allman, B.E., Jacobson, D.L., Arif, M., Werner, S.A. & Nugent, K.A. (2003) Quantitative phase radiography with polychromatic neutrons. *Phys. Rev. Lett.*, **91**, Art. no. 145502.

Meyer-Arendt, J.R. (ed.) (1992) *Selected Papers on Schlieren Optics: SPIE Milestone Series*, vol. MS61. The International Society for Optical Engineering, Bellingham.

Montgomery, W.D. (1968) Algebraic formulation of diffraction applied to self-imaging. *J. Opt. Soc. Am.* **58**, 1112–1124.

Montgomery, W.D. (1969) Distribution formulation of diffraction. The monochromatic case. *J. Opt. Soc. Am.* **59**, 136–141.

Montgomery, W.D. (1981) Unitary operators in the homogeneous wave field. *Opt. Lett.* **6**, 314–315.

Nazarathy, M. & Shamir, J. (1980) Fourier optics described by operator algebra. *J. Opt. Soc. Am.* **70**, 150–159.

Nesterets, Ya.I. & Punegov, V.I. (2000) The statistical kinematical theory of X-ray diffraction as applied to reciprocal-space mapping. *Acta Cryst.* **A56**, 540–548.

Nieto-Vesperinas, M. (1991) *Scattering and Diffraction in Physical Optics*. John Wiley & Sons, New York.

Nomarski, G. & Weill, A.R. (1955) Application à la métallographie des méthodes interférentielles à deux ondes polarisées. *Rev. Metall.* **2**, 121–128.

Nugent, K.A., Paganin, D. & Gureyev, T.E. (2001) A phase odyssey. *Physics Today*, **54**, 27–32.

Paganin, D., Mayo, S.C., Gureyev, T.E., Miller, P.R. & Wilkins, S.W. (2002) Simultaneous phase and amplitude extraction from a single defocused image of a homogeneous object. *J. Microsc.* **206**, 33–40.

Paganin, D. & Nugent, K.A. (1998) Noninterferometric phase imaging with partially coherent light. *Phys. Rev. Lett.* **80**, 2586–2589.

Paganin, D. & Nugent, K.A. (2001) Non-interferometric phase determination. *Advances in Imaging and Electron Physics* (ed. by P. Hawkes), pp. 85–127. Harcourt Publishers, Kent.

Papoulis, A. (1968) *Systems and Transforms with Applications in Optics*. McGraw-Hill, New York.

Peng, X., Yu, L. & Cai, L. (2002) Double-lock for image encryption with virtual optical wavelength. *Optics Express*, **10**, 41–45.

Saleh, B.E.A. & Teich, M.C. (1991) *Fundamentals of Photonics*. John Wiley & Sons, New York, sections. 2.2 & 4.1.

Snigirev, A., Snigireva, I., Kohn, V., Kuznetsov, S. & Schelokov, I. (1995) On the possibilities of X-ray phase contrast microimaging by coherent high-energy synchrotron radiation. *Rev. Sci. Instrum.* **66**, 5486–5492.

Somenkov, V.A., Tkalich, A.K. & Shil'stein, S. (1991) Refraction contrast in X-ray microscopy. *Sov. Phys. Techn. Phys.* **3**, 1309–1311.

Teague, M.R. (1983) Deterministic phase retrieval: a Green's function solution. *J. Opt. Soc. Am.* **73**, 1434–1441.

Weitkamp, T., Raven, C. & Snigirev, A. (1999) Developments in X-ray tomography II (ed. by U. Bonse). *Proc. SPIE*, **3772**, 311–317.

Wilkins, S.W., Gureyev, T.E., Gao, D., Pogany, A. & Stevenson, A.W. (1996) Phase-contrast imaging using polychromatic hard X-rays. *Nature*, **384**, 335–338.

Wilkins, S.W., Pogany, A., Stevenson, A.W. & Gureyev, T. (1997) *Phase retrieval in phase contrast imaging.* US patent #6226353 (Australian patent #716800) (24 December 1997; priority date 24 December 1996).

Yaroslavsky, L. & Eden, M. (1996) *Fundamentals of Digital Optics*. Birkhauser, Boston.

Younus, M.I. & Alam, M.S. (1999) Enhanced phase-stepped interferometry via appropriate filtering. *Opt. Eng.* **38**, 1918–1923.

Zernike, F. (1942) Phase contrast, a new method for the microscopic observation of transparent objects. *Physica*, **9**, 686–693.

Appendix: single-image phase-amplitude extraction

Consider a monochromatic scalar electromagnetic wave, the spatial part of which is described by the complex wavefunction $\psi(x, y, z)$, where x, y, z denotes a Cartesian coordinate system in three dimensions. Such a wavefunction can always be expressed as $\psi(x, y, z) = \exp(ikz)\tilde{\psi}(x, y, z)$, where $k = 2\pi/\lambda$, and λ is the wavelength of the radiation. When the radiation is paraxial, with a nominal direction of propagation given by the positive z-axis, the function $\tilde{\psi}(x, y, z)$ may be viewed as a perturbation of the elementary z-directed plane wave $\exp(ikz)$. This perturbation obeys the paraxial equation (Saleh & Teich, 1991):

$$\left(2ik\frac{\partial}{\partial z} + \nabla_\perp^2\right)\tilde{\psi}(x, y, z) = 0, \tag{A1}$$

where $\nabla_\perp^2 \equiv \partial^2/\partial x^2 + \partial^2/\partial y^2$ is the Laplacian operator in the x–y plane.

To obtain the associated continuity equation, write the complex wavefunction ψ appearing in Eq. (A1) in terms of its intensity $I \equiv |\tilde{\psi}|^2 = |\psi|^2$ and phase $\phi \equiv \arg\tilde{\psi}$; the imaginary part of the resulting expression yields the so-called transport-of-intensity equation (Teague, 1983):

$$-\nabla_\perp \cdot (I(x, y, z)\nabla_\perp\phi(x, y, z)) = k\frac{\partial I(x, y, z)}{\partial z} \tag{A2}$$

Assume that the intensity and phase in the plane $z = 0$ are related to each other via:

$$\phi(x, y, z = 0) = \alpha \log_e I(x, y, z = 0) + \varpi, \tag{A3}$$

where α and ϖ are dimensionless constants, and $I(x, y, z = 0)$ is non-zero over the region of interest. Apply $\Delta_\perp$ to both sides of Eq. (A3), substitute into Eq. (A2), make use of the approximation $\partial I(x, y, z)/\partial z \approx (I(x, y, \Delta z) - I(x, y, z = 0))/\Delta z$ (which will be valid if Δz is sufficiently small), and then re-arrange the resulting equation to obtain:

$$(1 - \gamma\nabla_\perp^2)I(x, y, z = 0) = I(x, y, z = \Delta z), \gamma \equiv \frac{\alpha\Delta z}{k}. \tag{A4}$$

A formal solution for $I(x, y, z = 0)$ may be written on inspection:

$$I(x, y, z = 0) = \frac{1}{1 - \gamma \nabla_{\perp}^2} I(x, y, z = \Delta z). \quad \text{(A5)}$$

Here, the symbolic operator $1/(1 - \gamma \nabla_{\perp}^2)$ is defined using the Fourier derivative theorem as $\hat{F}^{-1}(1/(1 + \gamma(k_x^2 + k_y^2)))\hat{F}$, where (k_x, k_y) are the Fourier space coordinates conjugate to the real space coordinates (x, y), and $\hat{F}$ denotes the Fourier transform operator with respect to x and y using the following convention:

$$\hat{f}(k_x, k_y) \equiv \hat{F}\{f(x, y)\} = \frac{1}{2\pi} \int_{-\infty}^{\infty} \int_{-\infty}^{\infty} \mathrm{d}x\, \mathrm{d}y\, f(x, y) \mathrm{e}^{-i(k_x x + k_y y)} \quad \text{(A6)}$$

for a sufficiently well behaved function $f(x, y)$. For a numerical implementation of the action of $1/(1 - \gamma \nabla_{\perp}^2)$ on data sampled over a discrete Cartesian lattice, one would typically make use of the fast Fourier transform in constructing $\hat{F}^{-1}(1/(1 + \gamma(k_x^2 + k_y^2)))\hat{F}$; this was done in the numerical analyses presented in the main text.

Equations (A3) and (A5) allow us to write down a formula for reconstructing the wavefunction $\psi(x, y, z = 0) = \tilde{\psi}(x, y, z = 0)$ in the plane $z = 0$, in the notation of Eq. (11):

$$\begin{aligned} &\psi(x, y, z = 0) = \hat{R}\{I(x, y, z = \Delta z), \boldsymbol{\tau} = (k, \alpha, \Delta z, \varpi)\}, \\ &= \mathrm{e}^{i\varpi} \left(\frac{1}{1 - \gamma \nabla_{\perp}^2} I(x, y, z = \Delta z) \right)^{i\alpha + \frac{1}{2}}, \gamma \equiv \frac{\alpha \Delta z}{k}. \end{aligned} \quad \text{(A7)}$$

As a special case of this formalism, assume a thin sample located in the plane $z = 0$, which is composed of a single material with position-dependent projected thickness $T(x, y)$ and complex refractive index, $n = 1 - \delta + i\beta$ (as mentioned in the main text, the absorption coefficient μ is related to β via $\beta = \lambda\mu/(4\pi)$. If the sample is sufficiently thin, and it is illuminated with z-directed coherent plane waves of intensity I_0, then the intensity and phase of the radiation at the exit surface of the sample is well approximated by:

$$I(x, y, z = 0) \approx \mathrm{I}_0 \exp(-\mu T(x, y)), \quad \text{(A8a)}$$

$$\phi(x, y, z = 0) \approx -k\delta T(x, y) + \phi_0, \quad \text{(A8b)}$$

where ϕ_0 is a constant. Equation (A8a) is the Beer–Lambert law of absorption, and the second quantifies the thickness-dependent phase shift suffered by the plane wave as it passes through the sample. Since Eq. (A8) obey Eq. (A3), with $\alpha = k\delta/\mu$ and $\varpi = \phi_0 - k\delta \ln I_0/\mu$, Eq. (A7) may be used to reconstruct $\psi(x, y, z = 0)$ from $I(x, y, z = \Delta z)$.

If the incident z-directed monochromatic plane waves are replaced with paraxial spherical waves emanating from an on-axis point upstream of the plane $z = 0$, then Eq. (A5) should be replaced by:

$$I(x, y, z = 0) = \frac{M^2}{1 - \gamma M^{-1} \nabla_{\perp}^2} I(Mx, My, z = \Delta z), \quad \text{(A9)}$$

where M denotes the geometric magnification (cf. Cowley, 1981). This yields a modified form of Eq. (A7) which, for the special case corresponding to Eq. (A8), leads to Eq. (13) of the main text.

For an alternative but less general account of aspects of this material, see Paganin *et al.* (2002).